

See discussions, stats, and author profiles for this publication at: <https://www.researchgate.net/publication/240475340>

# Tailoring Chemical Hardness in $\text{WO}_x - \text{ZrO}_2$ System

ARTICLE in CHEMISTRY OF MATERIALS · NOVEMBER 2006

Impact Factor: 8.35 · DOI: 10.1021/cm061251v

CITATIONS

10

READS

34

5 AUTHORS, INCLUDING:



**A. Iribarren**

Instituto de Ciencia y Tecnología de Material...

59 PUBLICATIONS 238 CITATIONS

SEE PROFILE



**Jorge A. Ascencio**

Universidad Nacional Autónoma de México

121 PUBLICATIONS 2,026 CITATIONS

SEE PROFILE



**Ariosto Medina**

Universidad Michoacana de San Nicolás de H...

55 PUBLICATIONS 269 CITATIONS

SEE PROFILE



**E. Torres-García**

Instituto Mexicano del Petroleo

43 PUBLICATIONS 748 CITATIONS

SEE PROFILE

## Tailoring Chemical Hardness in $\text{WO}_x\text{--ZrO}_2$ System

A. Iribarren,<sup>†</sup> G. Rodríguez-Gattorno,<sup>‡</sup> J. A. Ascencio,<sup>\*,§</sup> A. Medina,<sup>||</sup> and E. Torres-García<sup>\*,§</sup>

*Instituto de Materiales y Reactivos, Universidad de La Habana, Zapata y G. Vedado, Ciudad de La Habana 10400, Cuba; Centro de Investigaciones Avanzadas del IPN, Unidad-Mérida, Antigua Carretera Progreso Km 6, Apdo. Postal 73, Cordemex C. P. 97310, Mérida, Yucatan, México; Instituto Mexicano del Petróleo, Lazaro Cardenas 152, Col San Bartolo Atepehuacan México, Distrito Federal C.P. 07730, México; and Universidad Michoacana de San Nicolas de Hidalgo. Edificio U, C. U., Morelia, Michoacán. C. P. 58000, México*

Received May 29, 2006. Revised Manuscript Received August 30, 2006

Structural, optical, and chemical properties of the  $\text{WO}_x\text{--ZrO}_2$  nanometric system were investigated using Raman spectroscopy, high-resolution transmission electron microscopy (HRTEM), and UV–visible diffuse reflectance. From diffuse reflectance spectroscopy, the absorption profile of the species in which  $\text{WO}_x$  was present (layers and small clusters) on the surface of  $\text{ZrO}_2$  crystals was obtained. This study shows three main energetic regions for optical absorption. As tungsten (W) concentration diminished, which corresponded with a decrease in  $\text{WO}_x$  layer thickness, the absorption edge showed a blue shift, and the band gap increased. The analysis of such behaviors suggests that they are due to quantum confinement produced by 0- or 1-dimensional  $\text{WO}_x$  species. Local chemical analyses and HRTEM observations allowed determination of the presence of an irregular thin coating, a small cluster, and a crystalline thin film formation over the  $\text{ZrO}_2$  for samples with loadings of 6, 10, and 20 wt % of W, respectively. The results obtained from different techniques were used to propose a chemical approach to the relationship between structure and electronic behavior of the active surface as a function of W concentration.

### Introduction

It is well-known that the surface properties have an imperative role in the control of the catalysis process, related essentially with the changes in its acid–base properties. Furthermore, it is common to relate it with crystalline distribution or other factors involving structural configurations, such as preferential orientations, presence of individual elements, and so on, in the synthesized material. Structure manipulation has proved to be an important parameter to develop chemical reactivity. Composition, size, and structure affect the electronic distribution together with the atomistic configuration, producing significant variations in the chemical potential, which is related to the selectivity and activation energies during the catalyst design.<sup>1</sup> Besides, to have optimum materials for catalysts, it is indispensable to have the maximum effective area to induce reactions, which introduces a higher number of active sites per unit area and per unit volume. This is reached by reducing the dimension of materials to nanometric size, where size, composition, and structure have proved to be the parameters to modify the catalytic properties of a material candidate.<sup>2,3</sup>

Particularly, the  $\text{WO}_x\text{--ZrO}_2$  system has received much attention because of its good combination of activity and chemical selectivity. This is because of balanced surface acid properties, density of acid sites, and high thermal stability. This system brings the possibility for balancing the surface acid properties (density of acid sites) by varying the tungsten (W) content, which, combined with its high thermal stability, allows for high activities and selectivity in catalyzed reactions. When the  $\text{WO}_x\text{--ZrO}_2$  system was presented as a  $\text{WO}_x$  coating consisting of W clusters formed on the surface of  $\text{ZrO}_2$ , the following parameters were in place: (1) without the formation of detectable 3-dimensional  $\text{WO}_3$  crystallites when this system was synthesized by the impregnation method with loadings  $< \sim 15$  wt % W and (2) when it had a surface area of  $\sim 100 \text{ m}^2/\text{g}$ .<sup>4–6</sup> Other authors described the system as a structure of metastable tetragonal  $\text{ZrO}_2$  nanoparticles covered by a few-nanometers thick low-crystalline surface layer formed by the W oxospecies  $\text{WO}_x$ , which is obtained by selective precipitation and with concentrations of  $\sim 10$  wt % W.<sup>4,7</sup> More recently, direct evidence of the transformation of  $\text{WO}_x$  species in  $\text{WO}_3$  nanoclusters with orthorhombic structure in the  $\text{WO}_x\text{--ZrO}_2$  system has been

\* Address all correspondence to these authors. E-mail: etorresg@imp.mx (E. Torres-García) and ascencio@imp.mx (J. A. Ascencio). Phone: +52 55 91758430. Fax: +52 55 91758429.

<sup>†</sup> Universidad de La Habana.

<sup>‡</sup> Centro de Investigaciones Avanzadas del IPN.

<sup>§</sup> Instituto Mexicano del Petróleo.

<sup>||</sup> Universidad Michoacana de San Nicolas de Hidalgo.

(1) Jose-Yacamán, M.; Marin, M.; Ascencio, J. A. *J. Mol. Catal., A* **2002**, *14*, 3154.

(2) Narayanan, R.; El-Sayed, M. A. *J. Phys. Chem. B* **2005**, *109*, 12663.

(3) José-Yacamán, M.; Ascencio, J. A.; Liu, H. B. *J. Vac. Sci. Technol., B* **2001**, *19*, 1091.

(4) Barton, D.; Soled, S. L.; Meitzner, D.; Fuentes, G. A.; Iglesia, E. *J. Catal.* **1999**, *181*, 57.

(5) Boyse, R. A.; Ko, E. *J. Catal.* **1997**, *171*, 191.

(6) Barton, D.; Shtein, M.; Wilson, R.; Soled, S.; Iglesia, E. *J. Phys. Chem. B* **1999**, *103*, 630.

(7) Torres-García, E.; Rosas, G.; Ascencio, J. A.; Haro-Poniatowski, E.; Perez, R. *Appl. Phys. A* **2004**, *79*, 401.

reported.<sup>8</sup> However, the evidence until now reported is not determinant, and the characterization methods used usually present an uncertainty factor because the chemical composition is indirectly evaluated mainly for small layers of  $\text{WO}_x$  on the  $\text{ZrO}_2$  surface. With help of new techniques such as the transmission electron microscopy, particularly the linear chemical analysis on selected areas of the samples,<sup>9,10</sup> the study improved in quality, the results showed a significant increase in precision, and the contribution to the understanding of the phenomena was greater. The results of optical characterization traduced to chemical hardness were extended to the analysis of chemical behavior of this system in relation to catalyzed reactions.

Hence, in this work, experimental methods were used that allowed determining parameters such as size, structure, and composition during the evolution of the  $\text{WO}_x$  species on the surface of the  $\text{ZrO}_2$  depending on W content. These parameters permitted us to make correlations between the observed quantum size effects in the optical absorption and to establish its consequences in the electronic and chemical properties of the low-dimensional material obtained.<sup>11</sup>

### Experimental Methods

The  $\text{WO}_x\text{-ZrO}_2$  samples were prepared by impregnation of  $\text{ZrO}_{2-x}(\text{OH})_{2x}$  with ammonium metatungstate ( $(\text{NH}_4)_6\text{(H}_2\text{W}_{12}\text{O}_{40})\cdot n\text{H}_2\text{O}$ ) solution (Strem Chemicals, 99.9%) at pH = 10.<sup>12</sup> The whole mixture was stirred and heated to evaporate the water content in it, and this was followed by calcination in air for 3 h at 800 °C (tungsten content up to 30 wt %). High-surface-area  $\text{ZrO}_{2-x}(\text{OH})_{2x}$  (320  $\text{m}^2/\text{g}$ ) was prepared by hydrolysis of 0.5 M zirconyl chloride solution ( $\text{ZrOCl}_2\cdot 8\text{H}_2\text{O}$ , Aldrich, >98 wt %, Hf 0.5 wt %) with  $\text{NH}_4\text{OH}$  solution (Baker 28%) at pH = 10.<sup>13</sup>

After thermal treatment, the samples were characterized by diffuse optical reflectance spectra with a Varian (Cary 5E) spectrophotometer. The Kubelka–Munk function ( $F_{\text{km}}$ ) for infinitely thick samples was used to convert reflectance measurements ( $R_{\text{sample}}$ ) into equivalent absorption profiles using a reference reflectance, relating them to the absorption and scattering coefficients ( $\alpha$  and  $S$ , respectively):

$$F(R_{\infty}) = \frac{(1 - R_{\infty})^2}{2R_{\infty}} = \frac{\alpha}{S} \quad (1)$$

$$R_{\infty} = \frac{R_{\text{sample}}}{R_{\text{reference}}} \quad (2)$$

The Raman spectra were obtained in air at room temperature with a double monochromator Raman spectrometer (SPEX model 1403) using an  $\text{Ar}^+$  ion laser at a power

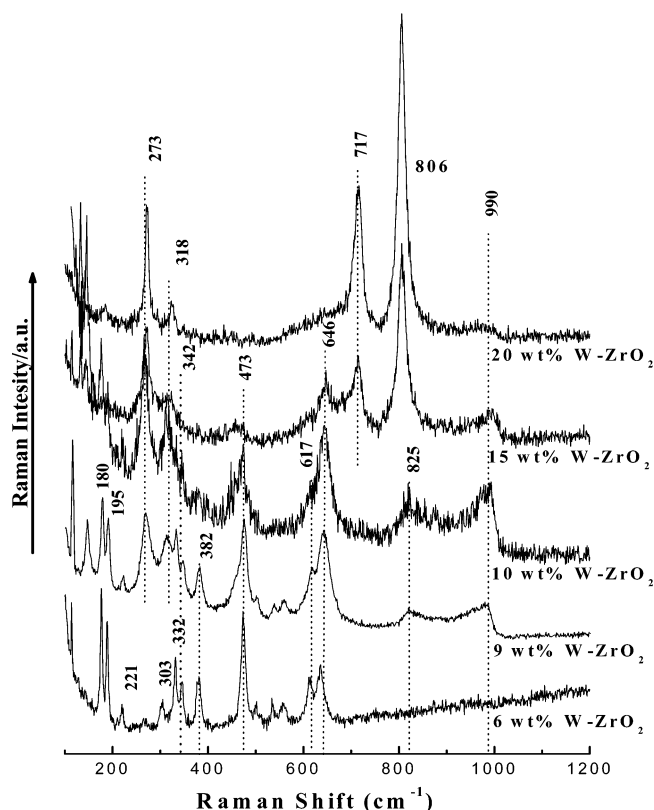


**Figure 1.** Typical Raman spectra of  $\text{WO}_x\text{-ZrO}_2$  samples as a function of the W loads on the surface of  $\text{ZrO}_2$ , calcined at 800 °C.

between 30–40 mW of incident radiation. The excitation line of the laser was 514.5 nm. The Raman signal was detected with a photomultiplier and a standard photon counting system.

Structural characterization was locally obtained with the help of a Tecnai F20 transmission electron microscope having an acceleration voltage of 200 keV, a field emission gun, and a minimal information limit of 1.5 Å. It also had an analytical system attached that allowed high-angle annular dark field (HAADF) for Z contrast images and obtained energy dispersive spectroscopy (EDS), including a line scan for elemental composition studies. Samples were prepared with a couple of drops on a copper grid with an amorphous carbon film. Optimum contrast and focused conditions were considered, and high-resolution images were obtained from local selected areas.

### Results and Discussion

**Raman Spectroscopy.** Raman spectroscopy was used to study the structure of  $\text{WO}_x\text{-ZrO}_2$  at a molecular length scale. Figure 1 shows the Raman spectrum of  $\text{WO}_x\text{-ZrO}_2$  samples, with different W loads on the surface.

The tetragonal and monoclinical  $\text{ZrO}_2$  polymorphs presented Raman bands in the 100–760  $\text{cm}^{-1}$  region, but not in the region of 800–1020  $\text{cm}^{-1}$ , where the main tungsten–oxygen bands were detected. The tetragonal  $\text{ZrO}_2$  can be identified from the bands at 318, 335, 382, 478, 550, and 646  $\text{cm}^{-1}$ , whereas the bands at 221, 315, 538, 560, and 617  $\text{cm}^{-1}$  are assigned to the monoclinical phase.<sup>14</sup>

- (8) Angeles-Chavez, C.; Cortes-Jácome, M. A.; Torres-Garcia, E.; Toledo-Antonio, J. A. *J. Mater. Res.* **2006**, *21*, 807.
- (9) José-Yacamán, M.; Ascencio, J. A.; Tehuacanero, S.; Marin, M. *Top. Catal.* **2002**, *18*, 167.
- (10) Dai, J. Y.; Li, K.; Lee, P. F.; Zhao, X.; Redkar, S. *Thin Solid Films* **2004**, *462*, 114.
- (11) Pearson, R. G. *J. Am. Chem. Soc.* **1988**, *110*, 2092.
- (12) Torres-Garcia, E.; Canizal, G.; Velumani, S.; Ramírez-Verdusco, L. F.; Murrieta-Guevara, F.; Ascencio, J. A. *Appl. Phys. A* **2004**, *79*, 2037.
- (13) Torres-Garcia, E.; Peláiz-Barranco, A.; Vázquez-Ramos, C.; Fuentes, G. A. *J. Mater. Res.* **2001**, *16*, 2209.

- (14) Jouanne, M.; Morhange, J. F.; Kanehise, M.; Haro-Poniatowski, E.; Fuentes, G. A.; Torres, E.; Hernandez-Tellez, E. *Phys. Rev. B* **2001**, *64*, 155404.

Raman spectra of supported species are generally interpreted by analogy to the characteristic Raman frequencies of reference compounds either in solution or in the solid state. Isopolytungstate compounds, consisting of  $[\text{WO}_6]$  octahedra, possess bands in the  $740\text{--}1000\text{ cm}^{-1}$  range (W–O symmetric and W–O–W antisymmetric stretching frequencies) and in the  $200\text{--}550\text{ cm}^{-1}$  range (W–O–W symmetric stretching and bending modes).<sup>15</sup> Monotungstate compounds, made up of  $[\text{WO}_4]$  tetrahedra, show bands in the range  $910\text{--}1061\text{ cm}^{-1}$  (W–O symmetric stretching) and in the range  $300\text{--}830\text{ cm}^{-1}$  (antisymmetric stretching and bending modes). The overlap in the Raman bands of the two symmetries and the distortions in both the tetrahedral and octahedral W–O groups that shift the band positions to high frequencies render the distinction between the different species very difficult.

Crystalline  $\text{WO}_3$  present intense and characteristic Raman bands at  $807$ ,  $717$ , and  $274\text{ cm}^{-1}$ , which are only present in the samples with loadings  $> 15\text{ wt } \%$  W and are absent from the spectra of samples with loadings  $< 15\text{ wt } \%$  W. This characteristic suggests the existence of a separate crystalline phase of  $\text{WO}_3$  for samples with loadings  $> 15\text{ wt } \%$ . The presence of the bands at  $970$  and  $985\text{ cm}^{-1}$  is attributed to surface tungsten species having various degrees of polymerization. On one hand, the bands at  $935$  and the broad band at  $829\text{ cm}^{-1}$  can be attributed with symmetric W=O stretching and to the antisymmetric stretching of the  $[\text{WO}_4]$  tetrahedra.<sup>16</sup> On the other hand, the shift of the bands of  $829\text{ cm}^{-1}$  to  $860\text{ cm}^{-1}$  is attributed to the existence of W–O–Zr stretching modes.<sup>8</sup>

The results described above suggest the presence of crystallized  $\text{WO}_3$  for the samples with loadings  $> 15\text{ wt } \%$  W, characterized by Raman bands at  $275$ ,  $717$ ,  $808$ , and  $985\text{ cm}^{-1}$ . The lack or low intensity and poorly resolved Raman bands, for samples with loadings  $< \sim 15\text{ wt } \%$  W, is characteristic of poorly crystallized samples and a high degree of the local disorder and suggests the existence of tungsten oxospecies highly dispersed on the surface as a  $\text{WO}_x$  coating. However, the experimental evidence obtained with Raman spectroscopy did not allow us to reach an unambiguous conclusion about the complete structure of this system. The self-limitations of an average measurement as produced by Raman spectroscopy imply the necessity of a well-localized study about the  $\text{WO}_x$  behavior on the  $\text{ZrO}_2$  surface.

**High-Resolution Transmission Electron Microscopy (HRTEM).** The use of transmission electron techniques allows for studying the differences between samples with different loadings and its consequences on the produced  $\text{WO}_x$  structure. Samples with loadings of  $6$ ,  $10$ , and  $20\text{ wt } \%$  W were compared using HRTEM images and elemental compositions obtained from linear scan analysis. Figure 2 corresponds to the sample with a  $6\text{ wt } \%$  W. In Figure 2a, a HAADF image of a section of the sample is shown where a nanostructured material is composed of multiple small clusters; it must be noticed that the contrast corresponds to a dark field-like image where the brightest regions correspond to an element with a higher Z number. Elemental composition

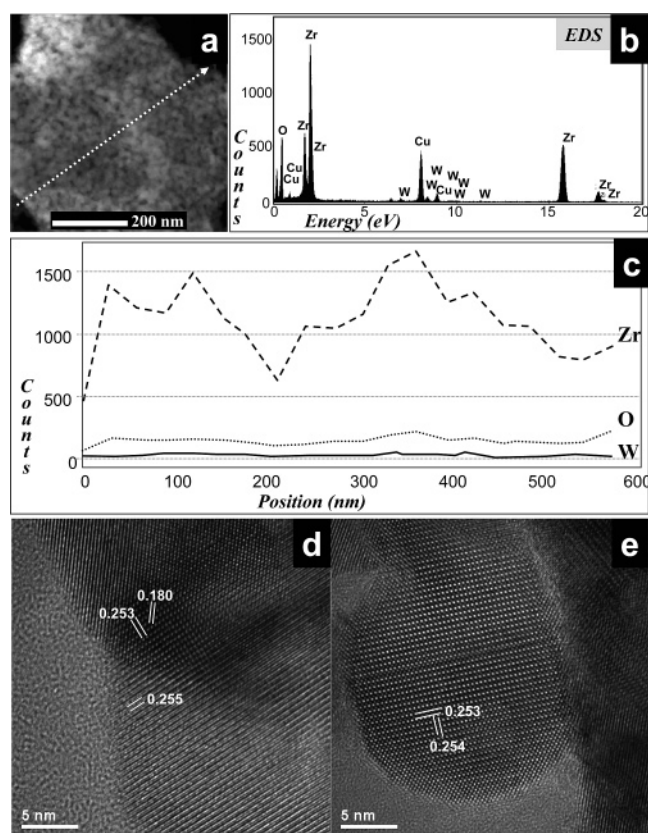


**Figure 2.** TEM analysis of a sample with  $6\text{ wt } \%$  W. (a) HAADF image of a nanostructured material composed of smaller particles, (b) EDS spectrum, (c) line-scan elemental composition from the arrow of (a), and a couple of HRTEM images (d and e) denoting bare and well-defined  $\text{ZrO}_2$  structures with tetragonal phase, as can be seen from the planar distance measurements.

tion of the whole region is characterized by EDS spectrum (Figure 2b), where the high concentration of Zr and O is clear (Cu appears as an effect of the grid composition), whereas just small evidence of W can be found. This element is found just as a trace in the sample. For a more localized analysis, a linear scan of characteristic X-ray signal was obtained along the marked arrow on the Figure 2a image, and the concentration is shown in Figure 2c. It is clear how Zr is the main element in the sample, and it diminishes in holes (zones where just the amorphous carbon of the grid is identified) of the sample. In addition, oxygen is present with low counts (this must be because of the atomic weight and the corresponding higher signal for heavier elements), whereas tungsten contribution is found with a low intensity, indicating its low concentration and its high dispersion.

The structure of the particles found in this sample is shown in parts d and e of Figure 2, where a couple of high-resolution micrographs are shown. In Figure 2d, two overlapped particles can be distinguished, one oriented parallel to the  $[001]$  axis with planar distances of  $0.253$  and  $0.180\text{ nm}$  that match the  $(200)$  and  $(220)$  planes of tetragonal  $\text{ZrO}_2$ .<sup>17</sup> In addition, a second one is oriented near  $[103]$ , where just the  $(200)$  planes can be distinguished. In Figure 2e, a particle is observed in the  $[001]$  orientation, where the contrast shows clearly a square distribution of dots. The HRTEM observa-

(15) Kuba, S. *Phys. Chem. Chem. Phys.* **2001**, *3*, 146.

(16) Gazzoli, D.; Valigi, M.; Dragone, R.; Marucci, A.; Mattei, G. *J. Phys. Chem. B* **1997**, *101*, 11129.

(17) Málek, J.; Benes, L.; Mitsushashi, T. *Powder Diffr.* **1997**, *12*, 96.



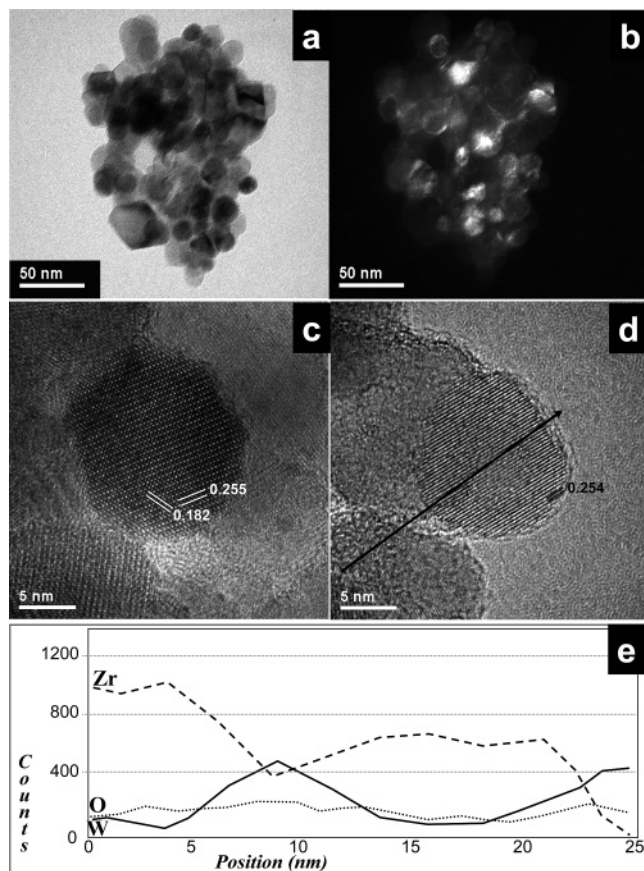


**Figure 3.** TEM analysis of a sample of  $\text{ZrO}_2$  with 10 wt % W. Low magnification (a) bright field and (b) HAADF images. HRTEM images of a couple of  $\text{ZrO}_2$  particles with  $\text{WO}_x$  around them (c and d) and (e) elemental concentration plot for the arrow in (d).

tions in this sample confirms that the  $\text{WO}_x$  species remains isolated along the  $\text{ZrO}_2$  surface as a well-dispersed and unordered phase as proposed by Iglesia and co-workers,<sup>6</sup> for low W contents.

Samples with 10 wt % W have a significantly different behavior and structure on the  $\text{ZrO}_2$  surface. The TEM study is shown in Figure 3, where a cluster of nanoparticles is observed in (a) a bright field and (b) HAADF images, where the regular morphologies of the  $\text{ZrO}_2$  particles and a smooth higher contrast around them can be observed. In higher magnification micrographs, the high-resolution contrast allows identifying particles at (c) [001] and (d) [013] orientation (as can be determined as the measured distances). In both micrographs, a thin layer of different material around the  $\text{ZrO}_2$  particles is found, which denotes that an amorphous film has been related to  $\text{WO}_x$ .<sup>7</sup> It must be noticed that there is also an effect on the particle surface, producing an irregular surface. However, even when previous reports have related the spacing of fringes with  $\text{WO}_3$ , the elemental composition has not been demonstrated completely. The use of line-scan with a small spot size allows identifying the composition over the arrow marked in the micrograph of Figure 3d. Even when the line-scan produces a delocalization error, the focused beam gives local information for the element that constitutes the sample.<sup>9,10</sup> In Figure 3e, the local chemical composition curve of a linear scan over a particle (see Figure 3d) shows a reduction of Zr content, whereas W increases at distances around 9 and 24 nm over the arrow, which match

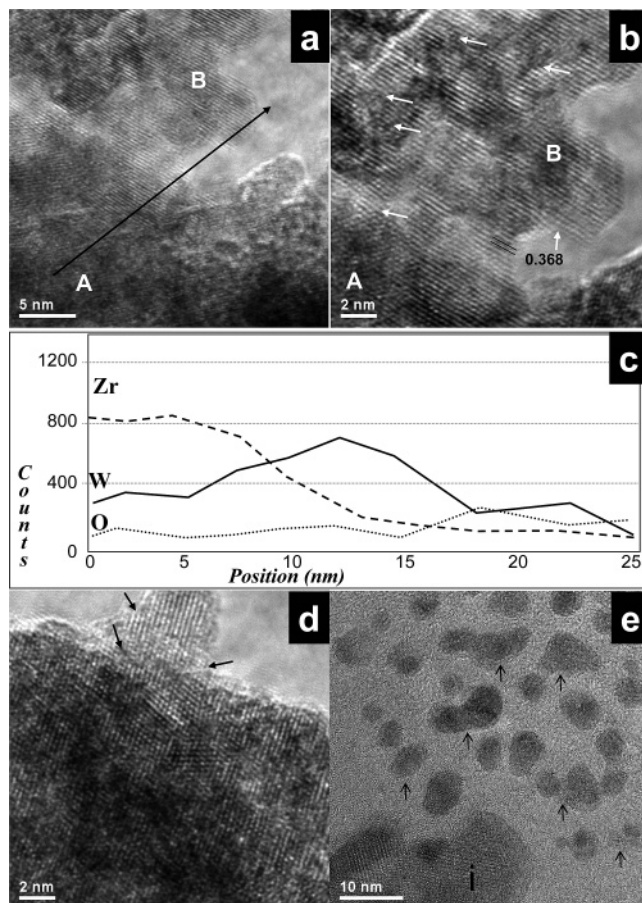


**Figure 4.** TEM analysis of a sample of  $\text{ZrO}_2$  with 20 wt % W. (a) Micrograph of two crystalline phases on the particle surface, and (b) a higher magnification of the  $\text{WO}_x$  crystal, with the corresponding (c) line-scan. HRTEM micrographs of (d) a particle aggregated to the  $\text{WO}_x$  layer in the surface of the structure and (e) multiple small nanoparticles of  $\text{WO}_x$  coalescence, induced by the own electron beam.

with the boundaries of the central particle in the image. This evidence demonstrates that the layer around the  $\text{ZrO}_2$  particles is composed mainly of W; however, the aggregation of these layers is basically constituted of an amorphous material coating all the  $\text{ZrO}_2$  particles. The formation of the  $\text{WO}_x$  layer on the  $\text{ZrO}_2$  could induce a local strain to the  $\text{ZrO}_2$  atomistic arrays, as has been reported for other types of interfaces.<sup>18,19</sup>

The corresponding analysis for the 20 wt % W shows different contrast and elemental compositions. In Figure 4a, a HRTEM image of two different crystalline phases is seen (marked with A and B, respectively); one of them is localized in the boundary of the material characterized by fringes with an inter-planar distance of 0.386 nm, as seen in the higher magnification of Figure 4b. This forms an irregular surface with well-defined facets. This measured spacing can be related to the planar distance of (010) of  $\text{WO}_3$ ; however, it can also be associated to the (110) family of planes of the tetragonal  $\text{ZrO}_2$ . Therefore, it is necessary to evaluate the elemental composition locally to determine the structure for each phase. A line-scan elemental composition plot is shown

(18) Litteken, C. S.; Stroband, S.; Dauskardt, R. H. *Acta Mater.* **2005**, *53*, 1955.

(19) Lee, H. Y.; Yu, Y. H.; Lee, Y. C.; Hong, Y. P.; Ko, K. H. *Appl. Surf. Sci.* **2004**, *227*, 244.

in Figure 4c, where the distribution of Zr is highly concentrated in the first 10 nm; the Zr signal is reduced while the corresponding to W increases. It must be noticed that oxygen remains low, but in the region where apparently there is no crystal, the O signal increases ( $\sim 18$  nm). Considering that the external crystal corresponds to tungsten oxide, a more careful analysis of Figure 4b allows identification of multiple defects in the parallel fringes; these defects are exemplified with the zones marked with arrows on the micrograph. This kind of defect can be associated to the coalescence process, produced by the aggregation of smaller particles,<sup>20–23</sup> and associated to local recrystallization processes. In a different region of the sample (Figure 4d), a zone with a smaller  $\text{WO}_x$  layer can be found, but with a protuberant as an added particle to the border, where the type of defects observed in the bigger layer is marked with an arrow. This appears as early-stage evidence of the layer formation, which can be generated by the coalescence of smaller  $\text{WO}_x$  nanoparticles that partially melt the  $\text{ZrO}_2$  surface covering. This wetting behavior has been reported for crystals generated at high temperature, when small clusters act as precursors. Searching near this zone, a big amount of  $\text{WO}_x$  particles was found (see arrows), which were in the middle of a coalescence process and formed bigger crystals that are marked as (i). Coalescence requires a low energy, which in this case was invested by the electron beam energy, but during the synthesis, the temperature was increased gradually.

It must be noticed that the self-coating mechanisms observed in the sequence allow for determination of an isolated W material when the load is low (6 wt % W). When it is increased, it forms thin films with dimensions that must involve quantum size effects (QSE), because it is constituted by just a few atomic layers (10 wt % W). This quantum confinement must be reduced when clusters of  $>2$  nm are formed (20 wt % W), where it is well-known that QSE are significantly reduced. This structural behavior induces an important change not only in the optical and electronic properties but also to the chemical affinity and the corresponding catalytic activity. Therefore, it is important to evaluate if these effects can be assumed even with the presence of the  $\text{ZrO}_2$  crystals, which could reduce the macroscopic evidence of these local effects. Thus, the use of optical absorption becomes crucial for the understanding of the material and its corresponding properties.

**Analysis of Absorption Edge Energy.** As shown in Figure 3, it was found that the material with a load of 10 wt % of W is composed of  $\text{ZrO}_2$  nanometric particles, surrounded by a shell-like  $\text{WO}_x$  layer. The low-crystalline surface layer on  $\text{ZrO}_2$  particles denotes an amorphous film related to  $\text{WO}_x$ . In samples with 20 wt % W,  $\text{WO}_3$  crystalline clusters were observed, in addition to the  $\text{WO}_x$  shell layer, as shown in Figure 4. This is in agreement with our Raman

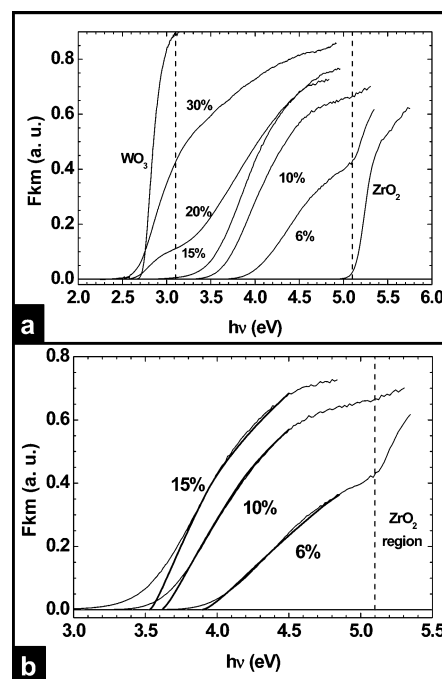


**Figure 5.** (a) Absorption profiles dependence on W concentration. The absorption profile of  $\text{ZrO}_2$  core without  $\text{WO}_x$  shell is also shown. (b) Fitting of eq 3 to experimental absorption edges for samples with low W load.

results. The mean cluster diameter was estimated to be about  $(6 \pm 1)$  nm.

Figure 5a shows the absorption edges of the  $\text{WO}_x$  samples for different W loads. Three main regions can be differentiated: (i) the low-energy region where  $\text{WO}_3$  bulk absorption predominates, (ii) the intermediate-energy region where the quantum confinement predominates, and (iii) the high-energy region where the  $\text{ZrO}_2$  bulk predominates. These regions are delimited in Figure 5a by dashed lines at  $h\nu = 3.1$  eV and  $h\nu = 5.1$  eV. In the low-energy region, corresponding to high W concentration ( $W \geq 15\%$ ), the typical  $\text{WO}_3$  bulk-like response predominates. The absorption edge in this zone is related to the formation of big  $\text{WO}_3$  crystallites at high W loads, which coincides with the Raman results and HRTEM images. In the intermediate-energy region, the oxospecies profiles predominate and show an energy shift due to quantum confinement. For low W loads, which correspond with high shifts, the profiles overlap with that of the  $\text{ZrO}_2$  core.

The energy dependence of the absorption coefficient ( $\alpha$ ) for semiconductors near the absorption edge is given by a general expression, which takes into account the transition type,

$$\alpha(h\nu) \propto \frac{(h\nu - E_g)^m}{h\nu} \quad (3)$$

where  $m = 1/2$  for direct transitions and  $m = 2$  for indirect ones. For determining the type of transition, the plot  $(\alpha h\nu)^m$  vs  $h\nu$  must present a linear behavior with  $m = 2$  if transitions are indirect and  $m = 1/2$  for direct transitions (see Figure 5b). The band gap energy  $E_g$  of the sample absorption profiles was calculated by extrapolating  $(Fkm h\nu)^m$  to 0.

The transition type in  $\text{WO}_x$  has been proposed in the literature to be either indirect<sup>6</sup> or direct.<sup>16</sup> In the  $\text{WO}_3$  region,

- (20) Liu, H. B.; Jose-Yacamán, M.; Perez, R.; Ascencio, J. A. *Appl. Phys. A* **2003**, 77, 63.
- (21) Ascencio, J. A.; Perez-Alvarez, M.; Tehuacanero, S.; Jose-Yacamán, M. *Appl. Phys. A* **2001**, 73, 295.
- (22) Sehayek, T.; Lahav, M.; Popovitz-Biro, R.; Vaskevich, A.; Rubinstein, I. *Chem. Mater.* **2005**, 17, 3743.
- (23) Vystavel, T.; Koch, S. A.; Palasantzas, G.; De Hosson, J. T. M. *J. Mater. Res.* **2005**, 20, 1785.



the best fitting absorption edge corresponds to  $m = 2$ , i.e., indirect transition. The resulting  $E_g$  is shown in Figure 5a, where it can be observed that the values have a mean energy  $E_g = (2.62 \pm 0.04)$  eV, which agrees with previous reports.<sup>24,25</sup> These results are associated to the absorption of the big WO<sub>3</sub> crystallites. This edge diminishes as W load increases and does not increase for W loads < 15 wt % W.

In the intermediate-energy region, a second absorption edge arose, which shifted to higher energies as the W load diminished, as can be observed in Figure 5a, although they are not sharp. The shifts of the profiles that have been described are associated to either the formation of nonstoichiometric W oxospecies or quantum confinement. The loss of the steepness at the absorption edge is expected under structural and chemical disorder conditions and thickness fluctuations,<sup>26</sup> although the edge shift persists. In the samples used for this study, the best fit of the profiles corresponds to  $m = 1/2$ , which indicates direct transitions as previously proposed.<sup>16</sup>

Taking into account that the WO<sub>x</sub>-shell thickness varied in each sample, nonunique local band gap energy was expected for each W load and the absorption profiles were dependent on the thickness dispersion. Therefore, the resulting absorption profile depends on the local absorption profiles and is given by the expression

$$\alpha(h\nu) \propto \frac{1}{h\nu} \int_{R_0-\Delta}^{R_0+\Delta} [h\nu - E_g(R)]^2 R^2 dR \quad (4)$$

where  $R_0$  is the mean shell thickness and  $\Delta$  is the thickness dispersion. The factor  $R^2$  is related to the local shell volume differential.

For the analysis of the absorption profiles, two approximations were made: (i) that  $x = 3$ , i.e., the shell compound was WO<sub>3</sub> and the shift attributed to quantum confinement, and (ii) that there was a uniform WO<sub>3</sub>-shell thickness distribution.

For higher W loads, the profiles were processed by scaled subtraction of the indirect edge. A careful processing helped to maintain a fairly constant band gap energy for such high W loads with a mean band gap energy  $E_g = (3.78 \pm 0.01)$  eV, which agrees with that reported by Gazzoli et al.<sup>16</sup>

In Figure 6, the behavior of the absorption edge energies for direct and indirect transitions is shown. The insert displayed the direct-transition edge energies, where energy values were constant for high W loads and increased for low W loads. Using a linear fitting, the slope changed at  $\sim 12$  wt % W, which can be identified at the point where the cluster begins to form as W load increases.

For pure ZrO<sub>2</sub> particles, shown in the high-energy region of parts a and b of Figure 5, the transition energy was  $E_{g,ZrO_2} \approx 5.20$  eV, which agrees with that reported by Barton et al.<sup>6</sup> in similar WO<sub>x</sub>–ZrO<sub>2</sub> system samples. For  $h\nu \geq 5.1$  eV, the absorption edge corresponding to ZrO<sub>2</sub> overlapped the WO<sub>x</sub> absorption profiles and showed a change of profile.

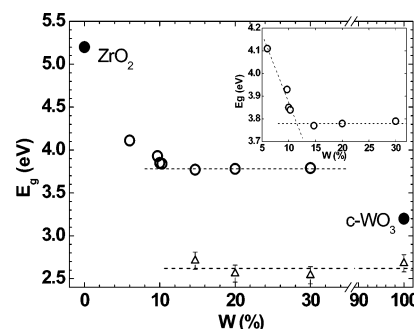


**Figure 6.** Direct (O) and indirect (Δ) absorption edge energies as a function of the W load. The insert details the variation of the direct absorption edge energies. Bulk WO<sub>3</sub> and ZrO<sub>2</sub> band gap energies are presented for comparison.

The ZrO<sub>2</sub> influence region is clearly delimited from the dotted line at  $h\nu = 5.1$  eV, as indicated in parts a and b of Figure 5.

If the results of HRTEM observations, Raman, and optical response are combined, it can be stated that, near the WO<sub>x</sub>–ZrO<sub>2</sub> boundary, a nonstoichiometric and low-dimensional WO<sub>x</sub> layer having high structural disorder surrounds the zirconia nanoparticles in which the interaction of W–O–Zr bonds must predominate. But, when the WO<sub>x</sub> thickness or cluster size increases, the ZrO<sub>2</sub> influence diminishes and polytungstate species appear (with increases of the terminal W=O bonds). The  $x$  index increases and tends toward  $x = 3$  far from the surface for sufficiently thick WO<sub>x</sub> layers.

The WO<sub>x</sub>–ZrO<sub>2</sub> system has been widely investigated as heterogeneous catalysts and particularly for this kind of study about oxidation reactions.<sup>12,27</sup> The fundamental understanding of the reduction potential or oxidizing power of WO<sub>x</sub>–ZrO<sub>2</sub> catalysts is very important for the rational design for selective oxidation reactions. The optical absorption edge energy represents the minimum energy required to excite an electron from the highest occupied molecular orbital (HOMO) in the valence band to the lowest unoccupied molecular orbital (LUMO) in the conduction band. Then, the band gap energy between the HOMO and the LUMO of a WO<sub>x</sub>–ZrO<sub>2</sub> catalyst can be related to its electronic hardness by applying the Koopmans' theorem to the well-known hardness definition developed by Pearson and Parr<sup>28–30</sup>, according to which

$$\eta = (\epsilon_{\text{LUMO}} - \epsilon_{\text{HOMO}})/2 = E_g/2 \quad (5)$$

where  $\eta$  is the hardness,  $\epsilon_{\text{LUMO}}$  and  $\epsilon_{\text{HOMO}}$  correspond to LUMO and HOMO energies, respectively, and  $E_g$  is the band gap. In the present case, the hardness is a function of shell thickness that is a result of the increase in electron localization due to electron confinement. Figure 7 shows calculated electronic hardness in the WO<sub>x</sub>–ZrO<sub>2</sub> system from band gap measurements. The fact that the electronic hardness can be conciliated only with the experimentally measured Lewis acidity in this system should be taken into account. As can be seen in Figure 7, the hardness decays exponentially when

(24) Ottaviano, L.; Lozzi, L.; Passacantando, M.; Santucci, S. *Surf. Sci.* **2001**, 475, 73.

(25) Bullett, D. W. *J. Phys. C: Solid State Phys.* **1983**, 16, 2197.

(26) Iribarren, A.; Menendez-Proupin, E.; Caballero-Briones, F.; Castro-Rodríguez, R.; Peña, J. L. *J. Appl. Phys.* **1999**, 86, 4688.

(27) Ramírez-Verduzco, L. F.; Torres-García, E.; Gómez-Quintana, R.; Gonzalez-Peña, V.; Murrieta-Guevara, F. *Catal. Today* **2004**, 98, 289.

(28) Pearson, R. G. *J. Chem. Educ.* **1999**, 76, 267.

(29) Parr, R. G.; Pearson, R. G. *J. Am. Chem. Soc.* **1983**, 105, 7512.

(30) Pearson, R. G. *J. Am. Chem. Soc.* **1963**, 85, 3533.

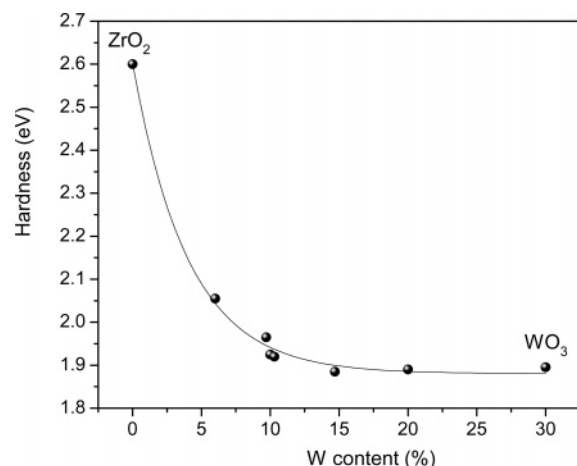


**Figure 7.** Calculated electronic hardness in  $\text{WO}_x\text{-ZrO}_2$  system from band gap measurements.

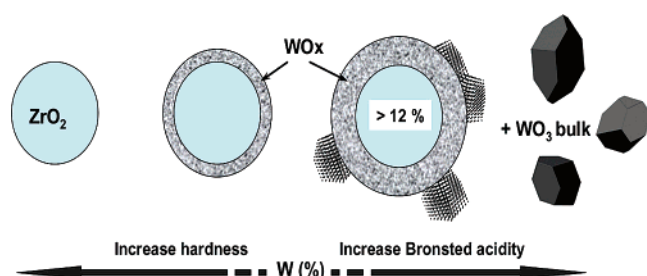


**Figure 8.** Schematic representation of  $\text{WO}_x\text{-ZrO}_2$  system evolution for different W concentrations.

the W content is increased up to a limit of  $\sim 12\%$ , which is essentially the same behavior as that of Lewis acidity obtained by adsorption measurements.<sup>31</sup> This behavior is expected because an increase of the  $\text{WO}_x$  shell should lead to a lowering of the electron confinement, as shown in the HRTEM observations. However, the estimated hardness does not include the Bronsted contribution to total acidity that, in the present system, has been shown to tend to increase monotonically with the increase in W content. Applications of the  $\text{WO}_x\text{-ZrO}_2$  system as catalyst usually show that there is a limit in which, for a certain value of W content, the maximum activity is reached.<sup>4,12,32</sup> The limits are always higher than the minimum hardness (the zone where  $\text{WO}_3$  start to appears as agglomerated phase besides core-shell:  $\text{WO}_x\text{-ZrO}_2$ ), indicating the necessity of increasing the local Bronsted acidity. Unfortunately, the Bronsted acidity can be only inferred from local softness,<sup>33,34</sup> and it cannot be directly related to total hardness. Equilibrium among acid Lewis and acid Bronsted sites (in mutual cooperation or not), for specific catalytic reaction, is an important key when tailoring the match between the reactants and catalyst chemical affinity.

Therefore, it is necessary to adjust the balance between both types of sites depending on the mechanistic aspects of the catalyzed chemical reaction.

Finally, based on HRTEM observations and UV-visible results, the  $\text{WO}_x\text{-ZrO}_2$  system can be presented as shown in the schematic in Figure 8. Increases of the W content cause the highly dispersed and disordered  $\text{WO}_x$  phase to increase in ordering and grow as a shell up to  $\sim 12\%$ , which subsequently segregates as crystalline  $\text{WO}_3$  particles. The HRTEM images previously shown are direct evidence of these phenomena.

## Conclusions

This study demonstrated that the  $\text{WO}_x\text{-ZrO}_2$  system is composed of  $\text{ZrO}_2$  nanometric particles, coated by a shell-like  $\text{WO}_x$  layer. The low-crystalline layer on the surface of  $\text{ZrO}_2$  particles indicates an amorphous film related to  $\text{WO}_x$  for the samples with W load up to 10 wt %, while  $\text{WO}_3$  nanoclusters with dimensions of  $\sim 6$  nm, besides the  $\text{WO}_x$  shell layer, were detected in samples where the load is  $> 15$  wt % W. Here, it is demonstrated that the surrounding material affects the properties of the samples. When the presence of a thin film of just a few atomic layers is observed, the structure of the samples is highly affected by the  $\text{ZrO}_2$  surface. When  $\text{WO}_x$  thickness is increased and big clusters are formed, the influence of the  $\text{ZrO}_2$  surface on the produced structure diminishes, and the polytungstate species tends to generate  $\text{WO}_3$ .

The optical study clearly shows three main regions: (i) the low-energy region (for  $h\nu \leq 3.1$  eV) where  $\text{WO}_3$  bulk influence predominates, (ii) the intermediate-energy region ( $3.1 \leq h\nu \leq 5.1$  eV) where the quantum confinement predominates, and (iii) the high-energy region where the  $\text{ZrO}_2$  bulk predominates (for  $h\nu \geq 5.1$  eV). Additionally, from analysis of the absorption edge energies for direct and indirect transitions, it was established that, around 12 wt % W, the clusters are produced from atomic surface diffusion and coalescence processes when W load increases.

Thus, the structural determination analysis, the optical absorption study, and the theoretical considerations allow for identification of the manner by which these materials modify their physicochemical properties during the coating layer. Depending on the tungsten load, thin films and the formation of small clusters are induced, denoting quantum size effect. It is evident that the best way to improve the performance of this catalyst and its properties involves the selection of a proper W load, which in turn depends on the chemical mechanism and application exigencies of a specific catalysis.

CM061251V

(31) Baertsch, C. D.; Komala, K. T.; Chua, Y.-H.; Iglesia, E. *J. Catal.* **2002**, 205, 44.

(32) Wen-dong, S.; Zhen-bo, Z.; Chuan, G.; Xing-kai, Y.; Yue, W. *Ind. Eng. Chem. Res.* **2000**, 39, 3717.

(33) Gázquez, J. L.; Méndez, F. *J. Phys. Chem.* **1994**, 98, 4591.

(34) Vetrivel, R.; Deka, R. Ch.; Pal, S. *J. Phys. Chem. A* **1999**, 103, 5978.